



Letters

Water storage capacity in olivine and pyroxene to 14 GPa: Implications for the water content of the Earth's upper mantle and nature of seismic discontinuities

Anaïs Férot, Nathalie Bolfan-Casanova*

Laboratoire Magmas et Volcans, Université Blaise Pascal, 5 rue Kessler, 63000 Clermont-Ferrand, France

ARTICLE INFO

Article history:

Received 27 July 2011

Received in revised form

6 June 2012

Accepted 12 June 2012

Editor: T. Spohn

Available online 11 August 2012

Keywords:

olivine

water storage

pyroxene

nominally anhydrous minerals

410 km

seismic discontinuities.

ABSTRACT

Experiments were performed under water-saturated conditions in the MFSH ($\text{MgO-FeO-SiO}_2\text{-H}_2\text{O}$) and MFASH ($\text{MgO-FeO-Al}_2\text{O}_3\text{-SiO}_2\text{-H}_2\text{O}$) systems at 2.5, 5, 7.5 and 9 GPa, at temperatures from 1175 to 1400 °C and H_2O initial abundance of 0.5–5 wt%. One experiment was performed at 13.5 GPa at a temperature of 1400 °C in the MFSH system. Water contents were analyzed by Fourier transform infrared spectroscopy. Results show that Al contents in olivine and pyroxene in equilibrium with an aluminous phase decrease significantly with increasing pressure and decreasing temperature. The incorporation of Al enhances water incorporation in olivine and pyroxene, but only at pressures of 2.5 and 5 GPa. At 7.5 GPa (i.e. 225 km depth) the pyroxene is monoclinic, indicating that in a hydrous mantle the orthoenstatite to clinoenstatite phase transition occurs at shallower depths than previously thought, which is more consistent with the Lehmann discontinuity than with the X discontinuity. The partitioning of water between pyroxene and olivine in the MFASH system decreases from a value of 2 at 2.5 GPa (80 km depth) to 0.9 at 9 GPa (270 km depth). At 13.5 GPa and 1400 °C, the water content of olivine is 1700 ± 300 ppm wt H_2O . The water partition coefficient between coexisting wadsleyite and olivine equals 4.7 ± 0.7 . We conclude that the water storage capacity of the upper mantle just above the 410 km discontinuity is of 1500 ± 300 ppm wt H_2O . If we assume that the Low Velocity Layer observed near 350 km is due to mantle melting, we can constrain the water content of the mantle at that depth to be $\sim 850 \pm 150$ ppm wt H_2O . This new value is four times higher than previous estimates for the mantle source of Mid Oceanic Ridge Basalts.

Finally, comparison of the depth ranges of the L and X seismic discontinuities and the water storage capacity of the upper mantle suggests that the L-discontinuity (180–240 km) is concomitant with a kink in the water storage due to the orthorhombic to monoclinic phase transition in enstatite, while the X-discontinuity (240–340 km) coincides with a kink in the water storage capacity due to dehydration of garnet.

© 2012 Elsevier B.V. All rights reserved.

1. Introduction

Trace amounts of hydrogen dissolved as point defects in nominally anhydrous minerals (NAMs) are believed to play a key role in physical and chemical processes in the Earth's upper mantle. Indeed, the distribution of water inside the mantle controls global mantle dynamics through the important effect of water on mantle viscosity (Hirth and Kohlstedt, 1996; Mei and Kohlstedt, 2000), solidus temperature (Gaetani and Grove, 1998; Aubaud et al., 2004) or phase diagrams (Frost and Dolejs, 2007; Deon et al., 2011). Hence, it is important to estimate the water

storage in mantle phases to constrain the deep water cycle and its effects on mantle melting and seismic signature.

Survey of water concentrations in natural minerals from mantle xenoliths shows that among NAMs, olivine is significantly less hydrous than pyroxenes (Bell and Rossman, 1992; Peslier et al., 2002; Bell et al., 2004). However, the application of measurements of natural olivines on the water content of the source region is questionable because of rapid hydrogen diffusion through olivine at high temperatures (Demouchy et al., 2006; see also Peslier, 2010 and references therein), leading to partial dehydration of olivine in mantle xenoliths during ascent (except apparently in kimberlitic samples). In addition, natural samples generally originate from shallow depths (maximum 250-km depth) and thus the water content in the deep mantle would be only accessible via remote sensing methods such as seismic observations or magneto-telluric measurements. Still, high-pressure and high-temperature experiments can provide information

* Corresponding author. Fax.: +33 4 73 34 67 44.

E-mail address: N.Bolfan-Casanova@opgc.univ-bpclermont.fr (N. Bolfan-Casanova).

on the equilibrium water solubility or water storage capacity of mantle olivine, which constitutes up to 60 vol% of the upper mantle mineralogy. Such data are important in order to constrain the water storage capacity of the upper mantle.

Numerous experimental data on water solubility in NAMs are available for upper mantle minerals, such as olivine (Kohlstedt et al., 1996; Mosenfelder et al., 2006; Zhao et al., 2004), pyroxenes (Rauch and Keppler, 2002; Mierdel and Keppler, 2004) and garnet (Lu and Keppler, 1997; Withers et al., 1998; Mookherjee and Karato, 2010). However, the majority of these studies are based on single phases, and at temperatures or pressures that are too low to be extrapolated to upper mantle conditions. Thus, models of water storage capacity in the mantle based solely on solubilities measured in simple systems and at lower temperatures are likely to be over-estimated (see Bolfan-Casanova, 2005). Indeed, contrary to low-pressure observations made at 0.3 GPa (Zhao et al., 2004), water solubility in olivine at high pressures decreases with increasing temperatures (Smyth et al., 2006; Litasov et al., 2007). With increasing depth silicates dissolve more and more into fluid water until formation of a supercritical fluid or melt (Stalder et al., 2001; Mibe et al., 2007). Thus, at high-pressures, the activity of water in melts decreases with increasing temperature and causes a decrease in water solubility in olivine. This effect was previously constrained (Bali et al., 2008) for melts coexisting with forsterite and enstatite at 2.5, 6 and 9 GPa and explains well the drop of solubility that was observed previously not only in olivine (Smyth et al., 2006; Litasov et al., 2007) and enstatite (Withers and Hirschmann, 2007), but also in wadsleyite (Demouchy et al., 2005) and ringwoodite (Ohtani et al., 2000, see Bolfan-Casanova, 2005 Fig. 2b for a review of existing data). In addition, the changes of composition and structure in pyroxenes should affect water partitioning with olivine and other minerals. Especially, it is expected that the water partitioning between olivine and pyroxenes will increase with depth due to the decrease of aluminum content in pyroxene with depth. However, this has never been constrained experimentally and previous estimates using low-pressure partitioning for the upper mantle may lead to overestimations of the pyroxene water contents.

The aim of this study is to constrain the combined effects of pressure, temperature and composition on water solubility in olivine and pyroxene under upper mantle conditions. Experiments were performed under water-saturated conditions in the MFSH (MgO–FeO–SiO₂–H₂O) and MFASH (MgO–FeO–Al₂O₃–SiO₂–H₂O) systems at 2.5, 5, 7.5 and 9 GPa, at temperatures from 1175 to 1400 °C and H₂O initial abundance of 0.5–5 wt%. One additional experiment was performed at 13.5 GPa and 1400 °C in the MFSH system.

2. Experimental procedures and analytical techniques

2.1. Starting materials

Water saturated experiments were carried out in the MFSH and MFASH systems. The starting material was made of a mixture of highly pure MgO and SiO₂ with FeO +/– Al₂O₃ powders and H₂O which was added as brucite Mg(OH)₂. MgO, SiO₂ and Al₂O₃ powders were annealed at 1000 °C overnight before weighting. FeO was incorporated as mixes of Fe and Fe₂O₃. The initial water content was variable from 0.5 to 5 wt% H₂O, depending on the pressure and temperature conditions and was controlled by incorporating different ratios of Mg(OH)₂ and MgO. Indeed, when pressure is increased, the amount of melt increases owing to the fact that it mixes a lot of water. Thus the bulk water content must be decreased to prevent extensive melting of the experimental charge. Olivine to enstatite ratios varied from 0.8 to 2, depending

on the pressure and temperature conditions. The mixed powder was homogenized in an agate mortar with ethanol and kept at 120 °C to avoid re-hydration.

2.2. High-pressure experiments

Experiments were performed from 2.5 to 13.5 GPa and 1175 to 1400 °C using the 1000-ton multi-anvil press fitted with a Walker type module at Laboratoire Magmas et Volcans (Clermont-Ferrand, France). The starting material was loaded into a Re folded capsule which in turn is placed into a Pt tube prior to welding. Inner Re capsule avoids iron loss and permits to buffer the oxygen fugacity by adding rhenium oxide at one end of the capsule. The Re–ReO₂ buffer is located between the Ni–NiO and magnetite–hematite buffers (Pownceby and O'Neill, 1994) and has the advantage of not reacting with the sample charge. Given that ferric iron solubility in olivine and enstatite is very low (O'Neill et al., 1996), the high oxygen fugacity should not affect the solubility of OH in these NAMs through interaction with Fe³⁺ (as seen in low-pressure olivines by Grant, 2007). Still, varying oxygen fugacity could change the speciation of H in the fluid/melt and hence change the activity of H₂O or OH. However, experiments conducted at 8 GPa and 1400 °C under varying conditions of *f*_{O₂} (from iron–wüstite to hematite–magnetite) show no systematic variation of water storage in olivine (Withers and Hirschmann, 2008). The capsule was surrounded by MgO, which acts as an insulator from the adjacent LaCrO₃ furnace, which in turn is thermally insulated by a ZrO₂ sleeve. In these assemblies, a stepped furnace is used in order to minimize thermal gradients. The pressure transmitting medium was made of MgO-octahedra doped with 5 wt% Cr₂O₃. Experiments at 2.5 and 5 GPa were carried out using 25 mm edge-length octahedra and WC-cube with 17 mm truncation length (25/17, 25M). Experiments at 7.5 and 9 GPa were performed in 18/11 (18M) assembly. Pressure was calibrated for both assemblies using known phase transitions of quartz/coesite and coesite/stishovite in SiO₂ (Zhang et al., 1996; Akaogi et al., 1995), garnet/perovskite in CaGeO₃ (Liu et al., 1991) and fayalite/spinel in Fe₂SiO₄ (Morishima et al., 1994). One additional sample was synthesized at 13.5 GPa using the 14/8 assembly (14M). Temperature was measured by Pt/PtRh₁₀ thermocouple in the 25M and by W₅Re/W₂₆Re thermocouple in the 18M and 14M assemblies, and monitored by a Eurotherm controller. Heating durations ranged from 5 to 50 h with the lower the temperature, the longer the heating time.

All the experiments were carried out under oxidizing conditions, confirmed by the simultaneous presence of Re and ReO₂ in the recovered capsule. The water saturation conditions were confirmed by the presence of free fluid after piercing the capsules. The capsules were then mounted in a UV light-cured composite to prepare doubly-polished thin sections for Fourier transform infrared (FTIR) spectroscopy analysis.

2.3. Analytical techniques

The textural relations within the capsule were achieved using a JEOL JSM-5910 scanning electron microprobe. The chemical compositions of olivine, pyroxene, aluminous phase and the quenched aqueous melt were recorded using a Cameca SX100 electron microprobe under operating conditions of 15 kV voltage and 15 nA current. 10, 20 and 50 s peak counting time were respectively used for analyzing Si, Mg, Fe and Al. Under such conditions for Al, the detection limit is of 0.015 wt% Al, that is ~0.0005 Al per formula unit. For the minerals, except wadsleyite, only data whose total was between 99 and 101 wt% were kept and normalized to 100 wt% (see Supplementary Tables 1 and 2). At such pressures, melts do not vitrify upon quenching, and thus

the melt compositions were measured using a defocused beam of 30–50 μm diameter depending on the size of the dendrites or by elementary mapping, and generally yield very low total owing to their porosity. Both techniques (wide beam or mapping) yield similar compositions whatever the size of the dendrites.

FTIR spectroscopy is a very useful and sensitive technique to quantify hydroxyl content in NAMs, which also gives structural information about H point defects. Polarized and unpolarized FTIR spectra were acquired using a Vertex70 Bruker spectrometer coupled to a Hyperion microscope equipped with $15\times$ objective and condenser. Beam size varied from 30 to 50 μm . The spectra were measured through a CaF_2 plate with a resolution of 2 cm^{-1} and up to 2000 scans were accumulated. The spectra were integrated between 4000 and 3000 cm^{-1} and OH content was quantified using the Beer–Lambert law. The integrated molar absorption coefficients of $28,450\text{ L moles H}_2\text{O}^{-1}\text{ cm}^{-2}$ (Bell et al., 2003), $80,600\text{ L moles H}_2\text{O}^{-1}\text{ cm}^{-2}$ and $38,300\text{ L moles H}_2\text{O}^{-1}\text{ cm}^{-2}$ (Bell et al., 1995) were used to calculate OH contents in olivine, orthopyroxene and clinopyroxene, respectively. For clinoenstatite, the absorption coefficient of Bell et al. (1995) used here has been recently confirmed by SIMS analyses (Withers and Hirschmann, 2007). For wadsleyite, an absorption coefficient of $73,000\text{ mol H}_2\text{O L mol}^{-1}\text{ cm}^{-2}$ was used (Deon et al., 2010). Density factors of 5358, 5448 and $4942\text{ L moles H}_2\text{O}^{-1}$ were used for olivine, pyroxene and wadsleyite respectively to convert water contents from $\text{moles H}_2\text{O L}^{-1}$ into ppm wt H_2O , using the formula $C(\text{ppm wt H}_2\text{O}) = C(\text{mol H}_2\text{O/L}) \cdot X$ with $X = 18/d \times 10^6$ and d the density of the phase (g/cm^3). We used the densities from the literature (olivine: Fisher and Medaris, 1969; pyroxene: Chai et al., 1997; HughJones and Angel, 1997; wadsleyite: Hazen et al., 2000). Given the limited compositional range of olivine and pyroxene in this study, there is little effect of the composition variation on density and hence on the density factors. For example, in olivine a change of 5% in the Fo content (i.e., the $\text{Mg}/(\text{Mg}+\text{Fe})$) leads to a change of only 2% in the density factor after calculation using the crystallographic data of Fisher and Medaris (1969). The same holds for orthopyroxene. Clinoenstatite having a similar density as orthoenstatite at room pressure (Angel and HughJones, 1994) the phase transition has no effect on the density coefficient.

Quantification of water content in anisotropic minerals using infrared spectroscopy requires to consider orientation effects. For olivine, we used polarized measurements on randomly oriented crystals. Two polarized spectra were acquired for each crystal at 0° and 90° of the extinction position as determined under crossed polars. In our previous study of water incorporation in forsterite (Bali et al., 2008), we successfully applied the method of Asimow et al. (2006). This method relies on comparison of the unknown spectra taken along perpendicular directions to those of an oriented standard polarized parallel to a , b and c to recalculate the spectra parallel to the three crystallographic axes, which can then be summed to yield the total absorbance (Libowitzky and Rossman, 1996). However, we found that this method is extremely sensitive to baseline correction, which probably also depends on iron content. Therefore we decided to use a different approach: knowing what the overtone bands of the silicate vibrations are along the crystallographic directions (located between 2200 and 1800 cm^{-1} , see Jamtveit et al. (2001) and Bali et al. (2008)), we detected three spectra which were as close as possible to the principal directions. The errors in the water contents measured by this method were calculated by measuring the relative difference between the overtone spectra of the unknown sample and the spectra representing the crystallographic axes of an oriented San Carlos olivine from Asimow et al. (2006). An example of comparison between polarized spectra measured on an un-oriented olivine from this study and

oriented olivine from San Carlos (from Asimow et al., 2006) can be seen in Fig. 8a. The mean percentage of error estimated for all olivine samples is around 20%. We also checked that the above method was accurate by analyzing unpolarized spectra. Indeed, it has been shown that the average of unpolarized measurements is equal to the total absorbance (as measured using polarized radiation) multiplied by three (Kovacs et al., 2008). We remind here that the above relationship is valid only in cases where the absorbance is low (below 0.3) or when the anisotropy is weak, that is when the ratio of the maximum polarized absorbance to the minimum polarized absorbance is close to one (Kovacs et al., 2008). Thus, there is a trade-off between water content and thickness in order to satisfy a condition of low absorbance that justifies the use of unpolarized radiation for quantification purposes. Given the thicknesses used in this study (average of $50\text{ }\mu\text{m}$) the trade-off is at around 1000 ppm wt H_2O . As shown in Supplementary Fig. S1, the water contents measured by the two methods align on a 1:1 trend, thus justifying the correctness of our method used to quantify olivine water content. Even the samples that display absorbances above 0.3 fall on the 1:1 trend. In the case of pyroxenes, all samples satisfied the low absorbance condition.

The water content in pyroxenes was also determined using polarized radiation. However, unlike for olivine, we did not know the spectra of the overtone bands along the principal directions. Thus, the three overtone spectra thought to represent the principal directions of orthopyroxene were identified using the features in the OH-region as known from the literature (see Supplementary Fig. S2). The γ direction satisfies the reported observation about the fact that OH absorption parallel to the c -axis represents $\sim 65\%$ of the total absorbance (Stalder, 2004). The three different overtone spectra identified for orthopyroxene were subsequently found to be in excellent agreement with those from Prechtel and Stalder (2012), the latter allowing to assign each direction to one of the crystallographic axes. Given the small difference in Raman active main bands between orthoenstatite and clinoenstatite, we assume that the infrared overtones for the principal directions were essentially the same for both polymorphs. The phase transition from orthorhombic to monoclinic in enstatite indeed does not seem to affect the quantification method adopted here, as shown in Supplementary Fig. S1. In this figure, we can see that the water content calculated from polarized spectra in the three principal directions equals the average from 10 unpolarized measurements multiplied by three (Kovacs et al., 2008). This is the case of pyroxenes synthesized at all pressures, whatever the structure, orthorhombic or monoclinic. The errors on pyroxene were calculated like for olivine and amount to an average of 37%.

In the case of wadsleyite, unpolarized measurements were performed on 10 separate grains because the samples were too thin to measure correctly the overtone spectra. The average of the unpolarized spectra was multiplied by three to obtain the total absorbance, following, again, Kovacs et al. (2008). Concerning garnets, they were too small ($\sim 5\text{ }\mu\text{m}$) to be successfully analyzed by FTIR.

3. Description of the samples

The samples in the MFSH system consisted of $(\text{Mg,Fe})_2\text{SiO}_4$ olivine and $(\text{Mg,Fe})\text{SiO}_3$ enstatite and a liquid phase. In the MFASH system olivine and enstatite are always in equilibrium with an aluminous phase, either spinel or garnet as illustrated in Fig. 1. At 2.5 GPa the aluminous phase is spinel, whereas at 5, 7.5 and 9 GPa the aluminous phase is garnet, in agreement with already reported spinel–garnet phase transition in peridotite

(Robinson and Wood, 1998). Using mass balance calculations, the proportion of the aluminous phase (spinel or garnet) increases with pressure, from less than 1% at 2.5 GPa, to 10% at 5 GPa, to

30% at 7.5 and 9 GPa. These values are slightly higher than values observed in peridotite system (for example ~20% garnet at 9 GPa, see Irifune and Isshiki (1998)). The aluminum content of pyroxene, olivine and liquid decreases with increasing pressure, which is compensated by the increase in aluminous phase proportion within the sample. The fraction of liquid increases with temperature in the MFSH and MFASH systems at each pressure as observed from mass balance calculations.

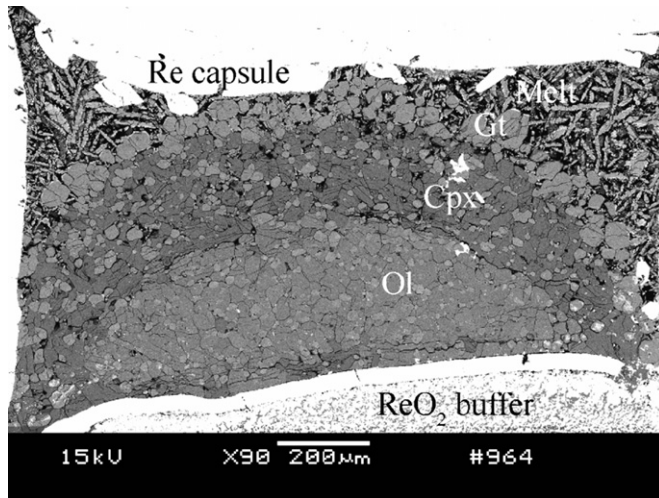


Fig. 1. Backscattered electron image of experimental charge #964 synthesized in the MFASH system at 7.5 GPa and 1250 °C. Ol: olivine, Cpx: clinopyroxene, Gt: garnet, Re: rhenium.

3.1. Chemical composition of the liquid phase

The melts become more mafic with increasing pressure (and also with decreasing temperature), as evidenced by the gradual increase of their molar ratio (Mg+Fe)/Si from approximately 1 at 2.5 GPa to about 3.5 at 9 GPa. This behavior is similar regardless of the system considered, and is comparable to what happens in the peridotite–water system (cf Kawamoto 2004), thus indicating that the dry composition of the supercritical fluids or melts observed in this study (in coexistence with olivine+pyroxene+garnet) are not very different from those in equilibrium with a more complex mantle mineralogy, especially presence of calcic-pyroxene. The water content of the melt was calculated by mass balance by normalizing the dry melt composition to 100% and by considering that water is extremely incompatible. The resulting water contents in the melts vary between

Table 1

Starting material, experimental conditions and chemical composition of olivine and pyroxene in the MFSH and MFASH systems. Water contents (ppm wt H₂O) displayed were determined by polarized FTIR measurements.

Sample	P (GPa)	Bulk water content (wt%)	T (°C)	Duration (h)	Olivine			Pyroxene			$D_{\text{px/ol}}^{\text{water}}$	$D_{\text{px/ol}}^{\text{watera}}$
					H ₂ O	Fo	X Al	H ₂ O	Mg#	X Al		
MFSH system												
#955	2.5	5	1175	44.5	126 (11)	92.6 (0.2)	–	101 (27)	93.5 (0.1)	–	0.80 (0.23)	–
#962		5	1250	46	54 (9)	92.6 (0.2)	–	58 (28)	93.6 (0.4)	–	1.08 (0.55)	–
#956		5	1325	44.5	32 (4)	93.2 (1.4)	–	25 (63)	95.7 (0.8)	–	0.78 (1.94)	–
#893b	5	2	1175	22.5	263 (26)	92.9 (0.2)	–	153 (44)	94.0 (0.2)	–	0.58 (0.18)	–
#895b		2	1250	18	286 (33)	92.2 (0.3)	–	81 (31)	93.1 (0.5)	–	0.28 (0.11)	–
#907		2	1400	19	18 (2)	95.7 (0.2)	–	10 (5)	96.5 (0.4)	–	0.53 (0.25)	0.44 (0.12)
#949	7.5	2	1175	42	2072 (461)	92.7 (0.2)	–	1331 (188)	94.2 (0.2)	–	0.64 (0.17)	0.58 (0.07)
#945b		2	1250	42	1262 (494)	92.3 (0.2)	–	777 (406)	93.9 (0.3)	–	0.62 (0.40)	0.71 (0.22)
#948b		2	1325	36	964 (479)	93.4 (0.2)	–	519 (318)	94.6 (0.2)	–	0.54 (0.42)	0.63 (0.10)
#1033		2	1400	31	830 (280)	92.7 (0.2)	–	593 (214)	93.9 (0.6)	–	0.71 (0.35)	–
#1043b	9	2	1175	30	4690 (1655)	91.8 (0.3)	–	2754 (0)	93.7 (0.3)	–	0.59 (0.21)	–
#1044b		2	1250	31	2805 (1071)	91.7 (0.4)	–	1244 (387)	93.4 (0.7)	–	0.44 (0.22)	–
#1047b ^b		2	1325	25.5	–	–	–	362 (67)	–	–	–	–
#1050b		2	1400	29.5	46 (6)	93.2 (0.6)	–	21 (8)	94.4 (0.8)	–	0.46 (0.19)	–
#1064b olivine	13.5	0.5	1400	5	1680 (300)	93.8 (0.3)	–	–	95.3 (0.4)	–	–	–
#1064b wadsleyite					7900 (700)	86.7 (0.3)	–	–	–	–	–	
MFASH system												
#922	2.5	5	1175	32	235 (44)	91.7 (0.4)	0.002 (0.001)	692 (229)	91.2 (0.5)	0.112 (0.010)	2.94 (1.12)	2.25 (0.48)
#923		5	1250	27.5	184 (52)	91.9 (0.5)	0.003 (0.001)	562 (237)	92.4 (0.4)	0.082 (0.007)	3.05 (1.55)	–
#957		2	1325	47	65 (12)	88.8 (1.5)	0.003 (0.001)	50 (34)	90.9 (1.9)	0.115 (0.030)	0.78 (0.54)	0.36 (0.16)
#954		2	1400	19	15 (2)	93.9 (0.7)	0.004 (0.001)	6 (2)	93.1 (2.2)	0.111 (0.047)	0.38 (0.15)	0.50 (0.34)
#893a	5	2	1175	22.5	–	94.2 (0.1)	0.001 (0.002)	607 (132)	94.6 (0.3)	0.047 (0.014)	–	–
#895a		2	1250	18	552 (56)	92 (0.2)	0.002 (0.001)	357 (122)	93.1 (0.3)	0.055 (0.010)	0.65 (0.23)	–
#1032a		2	1325	16	158 (29)	91.0 (0.5)	0.004 (0.001)	126 (54)	92.7 (1.1)	0.070 (0.011)	0.80 (0.37)	–
#1045		1	1400	27	129 (39)	94.7 (0.2)	0.005 (0.000)	169 (43)	94.0 (0.8)	0.082 (0.019)	1.31 (0.51)	–
#909	7.5	2	1175	18.5	904 (90)	94.0 (0.2)	0.000 (0.001)	707 (246)	94.3 (0.3)	0.014 (0.006)	0.78 (0.28)	0.78 (0.11)
#964		2	1250	42.5	876 (147)	91.3 (0.1)	0.001 (0.000)	884 (395)	92.8 (0.4)	0.006 (0.000)	1.01 (0.48)	0.86 (0.11)
#965		2	1325	31	593 (170)	90.3 (0.2)	0.001 (0.000)	514 (330)	91.7 (1.0)	0.006 (0.001)	0.87 (0.61)	0.99 (0.19)
#1049		2	1400	29.5	284 (70)	87.2 (0.5)	0.002 (0.004)	275 (74)	90.9 (0.3)	0.022 (0.004)	0.97 (0.35)	–
#1051	9	2	1175	50.5	1420 (380)	90.6 (0.1)	0.000 (0.000)	897 (750)	92.2 (0.8)	0.008 (0.001)	0.63 (0.55)	–

^a Water partition coefficient calculated from unpolarized infrared measurements on olivine and pyroxene.

^b Only pyroxene could be analyzed by FTIR in this experiment but the sample was lost before chemical analysis.

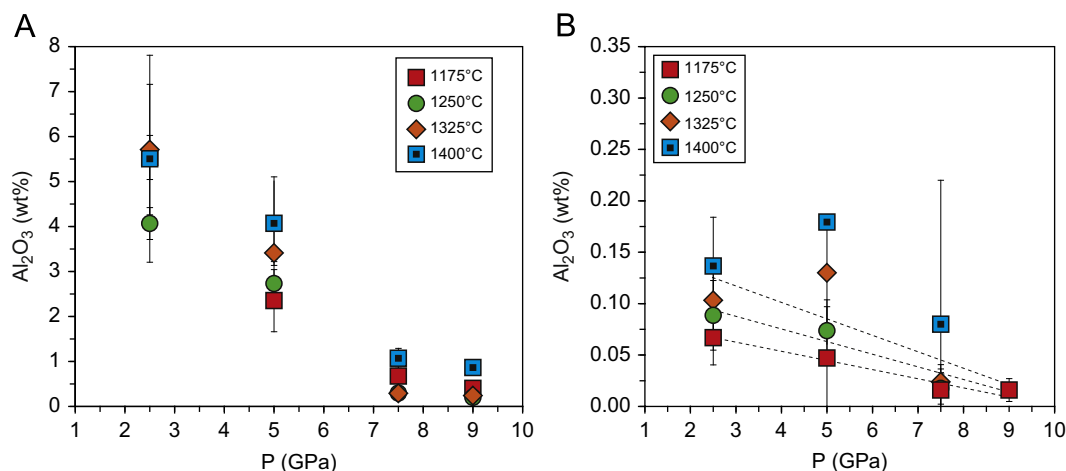


Fig. 2. Aluminum content (in wt%) as a function of pressure (GPa) in (A) pyroxene and (B) in olivine, in equilibrium with spinel or garnet at 1175, 1250, 1325 and 1400 °C. The error bars represent 2σ . The data for olivine synthesized at pressures of 7.5 and 9 GPa are at or below the detection limit.

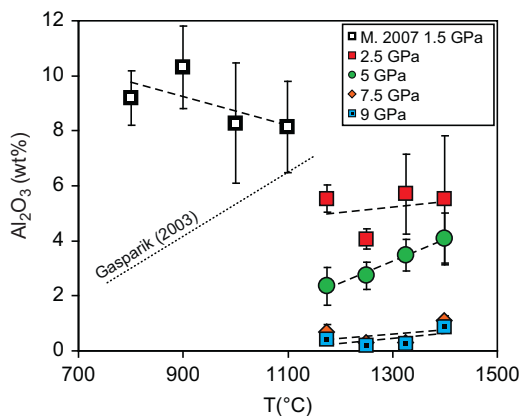


Fig. 3. Evolution of Al content in pyroxene synthesized in the MFASH system, in equilibrium with olivine and spinel or garnet. For comparison, data obtained at 1.5 GPa by Mierdel et al. (2007) in hydrous system are also shown (open squares). The model of Gasparik (2003) reflects the solubility of Al predicted in an anhydrous system (dotted line). The Al content in the pyroxene from this study behaves like in the dry system, indicating no substantial coupling between Al and H.

2 and 18 wt% H_2O and increase with increasing pressure as well as decrease with increasing temperature.

3.2. Chemical composition of the solid phases

The Fe, Al and water contents of the mineral phases are reported in Table 1. Complete compositional data set are given in the Supplementary Tables 1S and 2S. The Al contents in olivine and pyroxene in equilibrium with an aluminous phase strongly decrease with pressure and increase with temperature as shown in Fig. 2. Al contents in olivine vary from 0.02 to 0.2 wt% Al_2O_3 . Al incorporates preferentially into pyroxene with Al contents ranging from 0.3 to 5.7 wt% Al_2O_3 . For example, the Al_2O_3 content in pyroxene decreases from 5.5 wt% at 2.5 GPa and 1175 °C down to 0.4 wt% at 9 GPa and 1175 °C. In the present study, Al incorporates into pyroxene as a Tschermack component (i.e. $M^{2+} + Si^{4+} = 2Al^{3+}$, with $M = Mg^{2+}$, Fe^{2+}) similarly as in the dry system (Gasparik, 2003, see Fig. 3). Indeed, there is not enough dissolved water to observe coupling of H and Al (i.e., as in Mierdel et al. (2007) and Keppler and Bolfan-Casanova (2006)), probably because pressure is too high compared to the study of Mierdel et al. (2007). The decrease in Al content with increasing pressure is in agreement with previous reports (Tanner et al., 2009) and is well explained by the incorporation of Al into

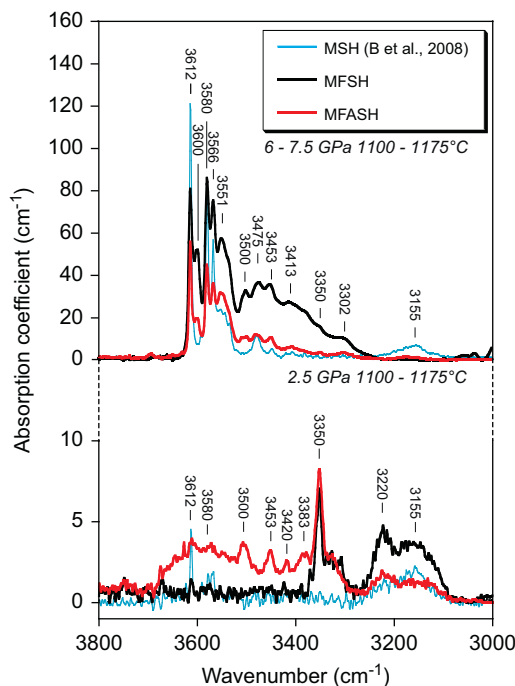


Fig. 4. Total infrared absorbance (as measured by summing the three components parallel to *a*, *b* and *c* crystallographic axes) representative of olivine in MSH (from Bali et al., 2008), MFSH and MFASH systems (from this study) at 2.5 GPa and 1100–1175 °C and 6–7.5 GPa and 1175 °C.

smaller Si sites which is strongly disfavored by a volume decrease upon compression. The effect of temperature on increasing Al content is also explained by the thermal expansion of the tetrahedral sites, which facilitates Al incorporation.

To the contrary of Al incorporation, the variation in iron content in orthopyroxene and olivine as a function of temperature is more complex and seems unsystematic. The iron content in pyroxene varies from 2.5 to 4.8 wt% FeO in the MFSH system and between 3.7 and 6.3 wt% FeO in the MFASH system. In olivine the FeO content varies from 4.3 to 8.1 wt% in the MFSH system and from 5.3 to 12.4 wt% in the MFASH system which correspond to Fo contents of 91.7–95.7 in the MFSH system and 87.2–94.7 in the MFASH system. The iron content varies little with pressure at a given temperature, but varies more systematically with temperature, probably controlled by its partitioning with the melt and/or garnet.

The garnet composition also changes with pressure with a pyrope component decreasing with pressure from 91% to 86%, almandine component increasing from 9% to 15% and a maximum majorite component of 5% at 9 GPa.

In the sample synthesized at 13.5 GPa and 1400 °C in the MFSH system, wadsleyite with Mg# (i.e., $\text{Mg}/(\text{Fe}+\text{Mg})100$) of 86.7 ± 0.3 coexists with olivine having a Mg# of 93.8 ± 0.3 .

4. Water contents

4.1. Olivine

At low pressures, i.e. below 5 GPa, the infrared spectra are governed by absorption bands located at low frequency (between 3000 and 3450 cm^{-1}). The number of bands increases as pressure increases due to the increase of H defect population with increasing water fugacity, especially bands at high-frequency appear (see Fig. 4). Above 5 GPa, the proportion of high-frequency bands (between 3450 and 3650 cm^{-1}) increases at the expense of those at low-frequency (between 3000 and 3450 cm^{-1}). While the spectra of low-pressure olivines (i.e. MSH by Bali et al. (2008), MFSH and MFASH systems) show different bands as a function of composition, the spectra of high-pressure olivines show all the same bands whatever the composition, although with some slight differences in the band intensities.

The band located near 3350 cm^{-1} was attributed to the presence of trivalent cations such as Fe^{3+} and Al^{3+} (Berry et al., 2007; Grant et al., 2007). This band occurs in the IR spectra of olivine synthesized in this study and its intensity decreases with increasing pressure, in agreement with the decrease in Al content of olivine with increasing pressure. Its intensity is quite low and does not exceed 10 absorption coefficient units. It represents generally below 5% of the total water content, except in sample 954 where it reaches 16%. Although the oxygen fugacity of the present experiments is high, the ferric iron content is unlikely to be high, as it has been shown that the solubility in olivine and orthopyroxene is low (below detection limit for olivine as shown by Mössbauer spectroscopy, O'Neill et al., 1996). Also, trivalent cation incorporation in both olivine and enstatite decreases with increasing pressure, as shown here for Al. Therefore, there is no reason to think that Fe^{3+} would behave differently. Finally, there are also some spectral hints in Fe-bearing enstatite that indicate low Fe^{3+} content (Stalder et al., 2005; see pyroxene section).

The overall IR band intensities decrease with temperature and increase with pressure. Bali et al. (2008) have shown that the solubility of water in forsterite follows a bell-shaped curve at 2.5, 6 and 9 GPa while water solubility measured in our experiments systematically decreases from 1175 to 1400 °C at 2.5, 5, 7.5 and 9 GPa (see also Smyth et al. (2006) and Litasov et al. (2007) for results at higher pressures). This is probably due to the fact that more chemically complex systems melt at lower temperatures. It

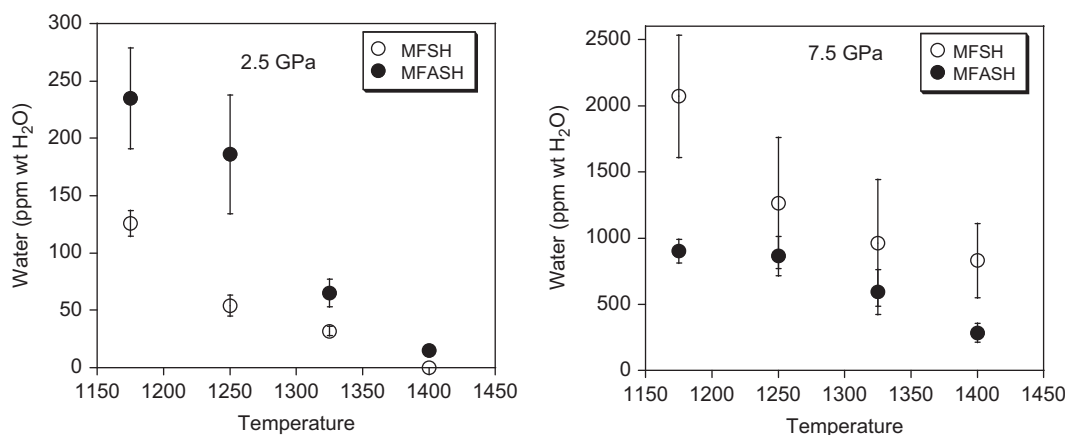


Fig. 5. Water content in olivine as a function temperature in the MFSH and MFASH systems at 2.5 and 7.5 GPa.

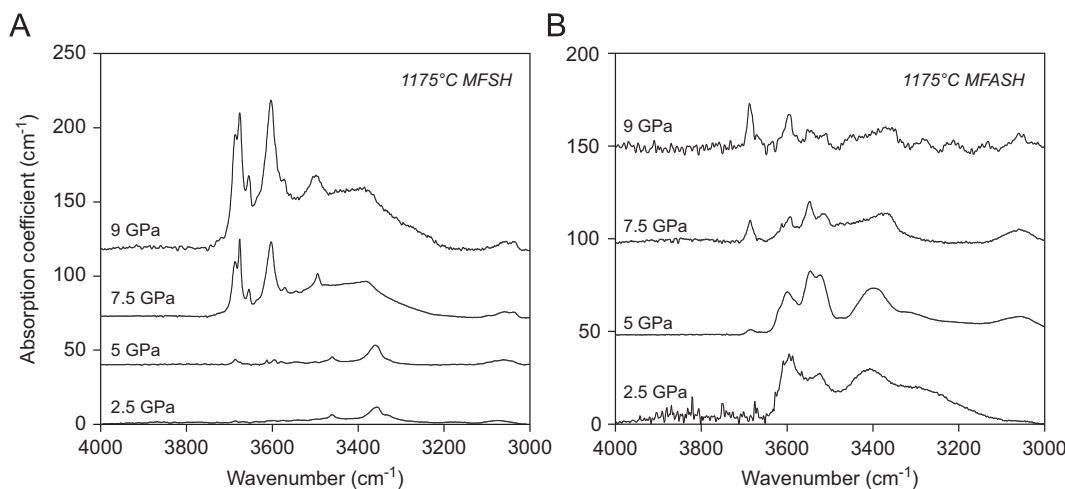


Fig. 6. Total infrared absorbance (as measured by summing the three components parallel to n_x , n_y , n_z) of pyroxene in MFSH (A) and MFASH (B) systems as a function of pressure at 1175 °C. Orthopyroxene at 2.5 and 5 GPa and clinopyroxene at and above 7.5 GPa.

follows that the water activity drop due to melting occurs at lower temperatures compared to the end member MSH system.

The incorporation of Al in the system enhances the incorporation of water in olivine, but only at 2.5 GPa. For example, at 2.5 GPa and 1175 °C the solubility of water in Al-bearing olivine is 235 ± 44 ppm wt H₂O while it is 126 ± 11 ppm in the Al-free olivine. The difference in water solubility reduces as temperature increases, even if the Al content increases with temperature (see Fig. 5). At 5 GPa and above 1300 °C the water content in Al-free and Al-bearing olivine equal each other. At 7.5 and 9 GPa, the presence of Al in the system limits the incorporation of hydrogen within olivine compared to the MFSH system. For example, at 7.5 GPa, water solubility in Al-free olivine decreases from 2072 ± 461 ppm wt at 1175 °C to 830 ± 280 ppm at 1400 °C, while in Al-bearing olivine it decreases from 904 ± 90 to 284 ± 70 ppm wt H₂O. This complex behavior can be explained by the change in concentration ratio of anhydrous Al defects/hydrous Al defects with increasing temperature, pressure and/or Al content (see Stalder et al., 2005).

To summarize, the effects of iron and aluminum on the solubility of water in olivine are complex and depend on conditions of temperature and pressure. However, at high-pressures (> 5 GPa), they remain minor compared to the important effect of water activity in the aqueous fluid.

4.2. Pyroxene

The spectra of orthopyroxene in the MFSH system are characterized by a broad band at ~ 3070 cm⁻¹ and a band at 3360 cm⁻¹ as already observed for enstatite by Stalder and Skogby (2002) and Rauch and Keppler (2002) (see Fig. 6). The spectra also display the additional bands due to iron incorporation located at 3328 and 3461 cm⁻¹, as observed by Stalder et al. (2005). The low intensity of the two latter bands compared to the major band at 3361 cm⁻¹ is indicative of low ferric iron contents. While, for $\text{Fe}^{3+}/\text{Fe}_{\text{total}} = 10\%$, the satellite bands display similar intensity compared to the one at 3361 cm⁻¹ band (Stalder et al., 2005).

In the MFASH system (Fig. 6) new bands appear at high frequency due to Al incorporation in agreement with Rauch and Keppler (2002) and Stalder (2004). At 7.5 GPa new bands in the MFSH system appear at frequency above 3400 cm⁻¹, whose intensity increases with increasing pressure (see also Bromiley and Bromiley (2006), for the pure MgSiO₃ system). Although we did not perform structural determination of the pyroxene in this study using Raman spectroscopy for example, the appearance of such bands is concomitant with the orthopyroxene to clinopyroxene transition localized at about 7 GPa between 1100 and 1400 °C as shown by Withers and Hirschmann (2007) in the hydrous MgSiO₃

system. The phase transition in the hydrous system occurs at 1.5 GPa below the transition in the anhydrous system (Angel and Hughjones, 1994), because the presence of water stabilizes clinopyroxene over orthopyroxene, in agreement with the higher water solubility in clinopyroxene compared to the one in orthopyroxene.

The presence of Al enhances water incorporation in pyroxene as shown in Fig. 7, but only at low pressures (2.5 and 5 GPa). At 7.5 GPa, the incorporation of water in MFSH and MFASH pyroxenes is similar. As for olivine, the water activity of the liquid is the predominant effect and controls the water solubility in pyroxene as a function of temperature.

4.3. Water partitioning between pyroxene and olivine

The effect of temperature on the water partitioning between pyroxene and olivine is negligible in both Al-free and Al-bearing systems except at 2.5 GPa as illustrated in Table 1 and Supplementary Fig. S3. Aluminum promotes the incorporation of water in pyroxene relative to olivine, but only at 2.5 GPa and at low experimental temperatures of 1175 and 1250 °C, where Al incorporation in pyroxene is the highest. Thus, under the conditions of most of the convective upper mantle (i.e. below 170 km depth), water will preferentially enter olivine than pyroxene. The data show that, above 5 GPa, the partition coefficient of water between pyroxene and olivine is mostly constant and ~ 0.9 and 0.5 in the MFASH and MFSH systems, respectively. Thus, a constant value of 0.9 was used for $D_{\text{pyroxene/olivine}}^{\text{water}}$ for the purpose of modeling the water storage capacity in peridotite. Such a partition coefficient is consistent with a partitioning of water between wadsleyite and olivine of 4.7 ± 0.7 (see below) obtained in this study and with the partitioning of water between wadsleyite and clinoenstatite of 5 obtained by Bolfan-Casanova et al. (in press) under the same conditions of pressure, temperature and oxygen fugacity. The $D_{\text{pyroxene/olivine}}^{\text{water}}$ obtained here is however lower than the value of 1.2 obtained by Tenner et al. (2012).

4.4. Water partitioning between wadsleyite and olivine

The IR spectra of olivine and wadsleyite coexisting in the sample synthesized at 13.5 GPa and 1400 °C are shown in Fig. 8. The olivine crystals were measured using polarized radiation, yielding 1680 ± 300 ppm wt H₂O. The wadsleyite crystals were measured using unpolarized radiation on 10 grains (and multiplied by a value of three, following Kovacs et al. (2008)), yielding 7900 ± 700 ppm wt H₂O. This wadsleyite displays a microprobe total of $98 \text{ wt}\% \pm 0.02$ and a $(\text{Mg} + \text{Fe})/\text{Si}$ ratio of 1.93 ± 0.01 based on 9 points of EMP analyses. These characteristics agree well with a water concentration comprised between 0.5 and 1 wt% H₂O as

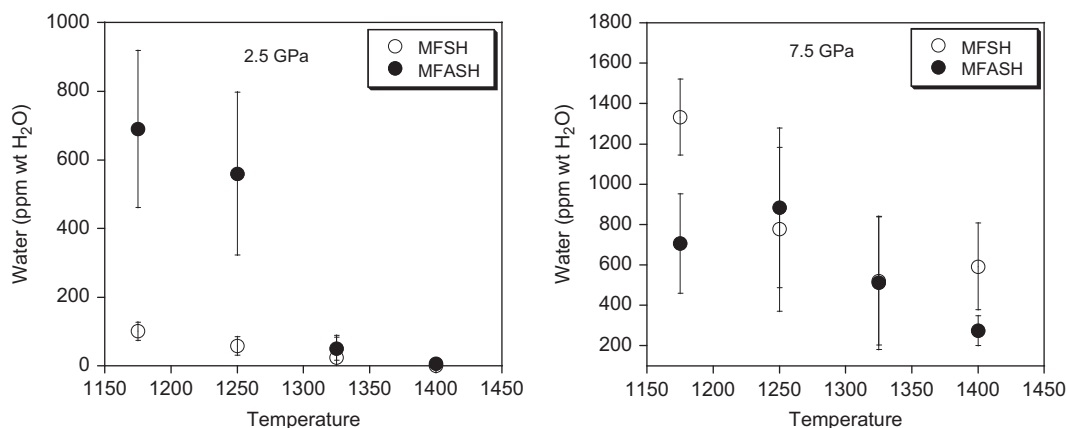


Fig. 7. Water content in pyroxene as a function of temperature in the MFSH and MFASH systems at 2.5 and 7.5 GPa.

measured here using the extinction coefficient of Deon et al. (2010) (see Inoue, 1994; Inoue et al., 1995). The water partition coefficient between wadsleyite and olivine is 4.7 ± 0.7 . This value is comparable to previous reports by Chen et al. (2002) and Deon et al. (2011) that measured a partition coefficient of water of 4.6–5.3 and 3.7 between wadsleyite and olivine in the MSH and MFSH systems, respectively, at 1200 °C. It has been suggested that the partitioning of water between wadsleyite and olivine decreases with increasing temperature (Frost and Dolejs, 2007; Litasov et al., 2011) on the basis of measurements made on $(\text{Mg,Fe})_2\text{SiO}_4$ olivine and Mg_2SiO_4 wadsleyite separately between 12 and 15 GPa by Smyth et al. (2006), Litasov et al. (2007), Litasov et al. (2011) and Demouchy et al. (2005). These separate measurements suggest a $D_{\text{wadsleyite/olivine}}^{\text{water}}$ of ~ 2 at 1400 °C. Still, to our knowledge, there is no other direct evidence concerning the partitioning of water between wadsleyite and olivine in iron-bearing system.

5. Water saturation curve in the Earth's convective upper mantle

The water saturation curve of the upper mantle is constructed starting from the measurements of the water solubility in olivine from this study. Temperature follows the geothermal gradient of convective mantle after Katsura et al. (2004). A potential temperature of 1277 °C was chosen because it is a good compromise between the estimate of potential temperature in the ocean ridges performed from the composition of MORB (McKenzie and Bickle, 1988) and the estimate by Katsura et al. (2004) who predicted a potential temperature between 1260 and 1350 °C according to the temperatures deduced from the transition zone pressure at 410 km. The model takes into account the change in phase proportion in peridotite with depth from Irifune and Isshiki (1998) and Irifune (1987). Except that in the present case the orthopyroxene disappears at shallower depths of 200–230 km due to stabilization of the monoclinic high-pressure polymorph by the presence of water (see discussion above). The model is built based on the following steps.

5.1. Water solubility in olivine

Given that the measurements of water solubility in olivine were performed at fixed temperatures of 1175, 1250, 1325 and 1400 °C (not necessarily corresponding to the geotherm) the water solubilities at temperatures of the geotherm were retrieved from interpolations of the data measured as a function of temperature at each pressure of 2.5, 5, 7.5, 9, 13.5 GPa (see Fig. 9). The water storage capacity of olivine follows an exponential curve in agreement with the thermodynamics of water incorporation in NAMs

$$[\text{OH}] \propto f_{\text{H}_2\text{O}}^n \exp(-\Delta G/RT) \quad (1)$$

with $n=1$ for olivine, which is the exponent corresponding to the substitution $2\text{H}^+ = \text{Mg}^{2+}$. Concerning the choice of n exponent, it should be noted that there is a controversy regarding the substitution mechanism of H in olivine. Indeed, since the study of Bai and Kohlstedt (1992, 1993), twenty years of research have not fully elucidated the mechanism of H incorporation in olivine. Initially, Bai and Kohlstedt (1992, 1993) identified two types of bands: group I ($3450\text{--}3650\text{ cm}^{-1}$) and group II ($3100\text{--}3450\text{ cm}^{-1}$). Based on the f_{O_2} dependence of the concentration of OH associated with each group, they speculated on H occupying Mg vacant sites or doubly charged oxygen interstitials for group I and H occupying Si vacant sites or singly charged oxygen interstitials for group II. The Mg vacancy mechanism was subsequently reinforced by solubility experiments as a function of pressure (Kohlstedt et al., 1996; Mosenfelder et al., 2006), but also by single crystal XRD measurements, that evidence vacancies essentially on the M1 site of olivine (Smyth et al., 2006; Kudoh et al., 2006). Following studies confirmed the distinction between the two groups of bands and observed a stronger effect of silica activity, with group I bands being more intense in MgO-buffered experiments while group II bands were more intense in pyroxene-buffered experiments. This led to the opposite conclusion that group I and group II bands are due to Si and Mg vacancies, respectively (Matveev et al., 2001; Lemaire et al., 2004; Berry et al., 2005; Kovacs et al., 2011). This latter conclusion is supported by recent first-principle calculations (Umemoto et al., 2011; Balan et al., 2011). In addition, electron microprobe

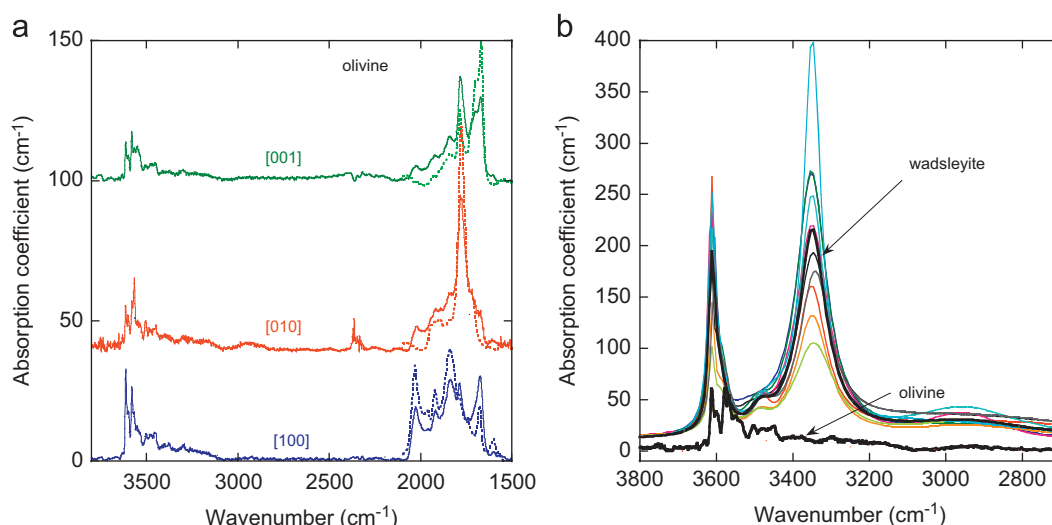


Fig. 8. FTIR spectra of olivine and wadsleyite coexisting in a sample made at 13.5 GPa and 1400 °C in the MFSH system. (a) The polarized spectra of olivine are shown together with the overtones from oriented San Carlos olivine (dotted curve from Asimow et al. (2006)). (b) Ten wadsleyite grains randomly oriented were measured with unpolarized radiation, the average of which is shown as the thick curve. Also shown in (b) is the absolute absorbance of olivine, representing the sum of the three spectra shown in (a). As the total integrated absorbances (or areas) of wadsleyite and olivine spectra differ by a factor of ~ 14 , while their absorption coefficient differ by a factor of 2.6, this leads to a water partitioning of $\sim 4\text{--}5$ between wadsleyite and olivine.

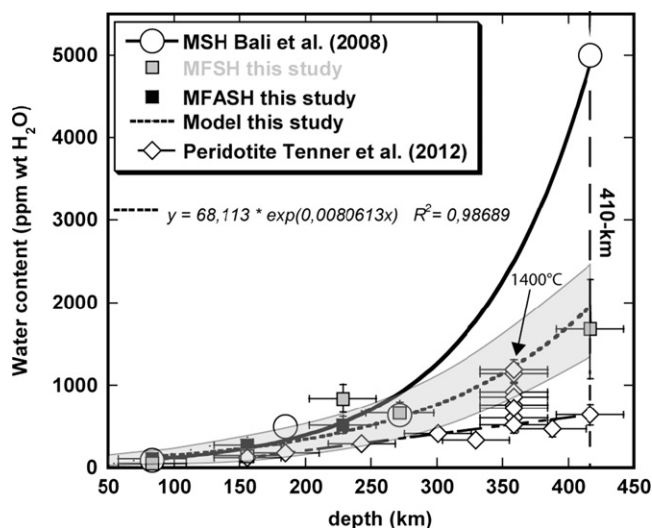


Fig. 9. Water storage capacity in olivine as a function of depth for different compositional systems. The solubility of water in forsterite (shown as empty circles and black curve) is from Bali et al. (2008). The gray area limits the upper and lower bounds of the water storage capacity in olivine following the geotherm temperatures (thick dashed curve, equation shown) as determined from the uncertainties in this study (black and gray squares). Also shown are the data from Tenner et al. (2012) at 1450 °C as diamonds which display a linear trend. At 360 km depth the vertical diamond symbols represent data from experiments performed as a function of temperature from the same study of Tenner et al. (2012). The arrow points out to their datum from 1400 °C, showing a good agreement with our results. See text for details.

measurements evidence some Si deficit in wet olivine synthesized at 12–14 GPa (Litasov et al., 2007).

Still, there is no need to decide which incorporation mechanism of H dominates in olivine in order to model its storage capacity using Eq. (1). If $n = 1$, the ΔV of the solid reaction is close to 10 cm³/mole, which is similar to the molar volume of MgO (see Keppler and Bolfan-Casanova, 2006), while if $n = 2$ (like in the case of the hydrogarnet substitution $4\text{H}^+ = \text{Si}^{4+}$) the ΔV calculated from the data of Kohlstedt et al. (1996) or Mosenfelder et al. (2006) would be close to 23 cm³/mole, which is similar to the molar volume of coesite. Both couples of (n , ΔV) equally fit the data and this disables any conclusions to be made regarding n equal to 1 or 2 except the fact that elasticity data (Smyth et al., 2006) point out to a molar volume change of 10 cm³/mole (Bali et al., 2008) calculated a ΔV of 11–11.7 cm³/mole for $\Delta V_{\text{solid}} = V_{\text{HydrousMg}_2\text{SiO}_4} + V_{\text{MgO}} - V_{\text{Mg}_2\text{SiO}_4}$. Anyway, whatever the thermodynamic quantities mean in terms of incorporation mechanism, what is important here is that they describe correctly the observations.

The model for water solubility in forsterite coexisting with enstatite and a fluid/melt in the MSH system as determined by Bali et al. (2008) at 2.5, 6 and 9 GPa is shown in Fig. 9. Also the datum of Smyth et al. (2006) at 12 GPa and 1400 °C is included. The solubility of water in olivine in the MFSH and MFASH systems is in the same order of magnitude as for forsterite up to 9 GPa (270 km depth) as illustrated in Fig. 9. At higher pressures, the storage of water in forsterite becomes much higher than that in olivine and reaches 5000 ppm wt H₂O at 410 km depth. This can be explained by two competing effects: the water solubility in olivine is higher than that in forsterite due to the enhancing effect of iron (Zhao et al., 2004; Withers et al., 2011), however in chemically more complex systems, the solidus is depressed, leading to a lowering of the water activity. We can thus expect that in peridotite, the water storage capacity of olivine could be lower than in the MFASH system. The recent data of Tenner et al. (2012) about water storage capacity of olivine equilibrated in a peridotite system are also shown in Fig. 9. Their data at

1450 °C plot along a linear trend reaching ~600 ppm wt of water in olivine at 416 km depth. However, they also report a storage capacity of 1190 ± 120 ppm wt at 1400 °C and 360 km depth that coincides with our storage curve. It is thus likely that the difference between our model of water storage capacity in olivine and that of Tenner et al. (2012) is due to a higher temperatures of 1450 °C, which explains their lower storage capacity.

5.2. Partitioning of water between pyroxene and olivine

As shown in Supplementary Fig. S3, interpolation of the data at 2.5 GPa in the MFASH system indicates that the water solubility in orthopyroxene is twice that of olivine at around 1300 °C. At pressures of 5, 7.5 and 9 GPa, and for temperatures of the geotherm, an average value of 0.9 in the Al-bearing system is observed and is thus used above 2.5 GPa. Withers et al. (2011) also evidence a decrease of partition coefficient from about 1.0 at 3 GPa to 0.65 at 6 GPa in the MFSH system. We do not consider any change of water partition coefficient between pyroxene and olivine through the orthorhombic/monoclinic transition in enstatite since we did not observe any, given the uncertainties. Concerning calcic pyroxene, there is no data at high-pressures and high-temperatures permitting to decipher if composition is or not important for the quantification of the storage capacity of Mg-clinopyroxene versus Ca-clinopyroxene. We consider that below the orthorhombic/monoclinic phase transition in enstatite the partitioning of water between high-Ca pyroxene and low-Ca pyroxene is 1.2 (see Tenner et al., 2009), while above the transition it becomes 1, i.e. both monoclinic pyroxenes store the same amount of water. Still, the modal volume of this phase does not exceed 12% in a peridotitic assembly (Irfune and Isshiki, 1998) at 410 km depth.

5.3. Water solubility in garnet

The model takes into account the water solubility in pyrope-rich garnet, based on recent data by Mookherjee and Karato (2010) obtained at 1100 °C. In order to extrapolate these data to mantle temperatures, the water concentrations were corrected for the water solubility drop at high temperatures using the parameterization of water activity in the fluid along the geotherm from Bali et al. (2008) (see Supplementary Fig. S4). The water activity of the fluid, as estimated by Bali et al. (2008), arises from data obtained in the MSH system, however it is likely that the water activity in a fluid/melt coexisting with peridotite is much lower than that in the MSH system, in which case the water solubility in garnet should be even lower. Thus, it is possible that our model overestimates the water storage capacity of garnet and it is necessary to explore the behavior of garnet/majorite at higher pressures with respect to water storage. For example, Bolfan-Casanova et al. (2000) report 600 ppm wt H₂O in MgSiO₃ majorite synthesized at 17 GPa and 1500 °C. Integrating this value into the water saturation curve, using a modal proportion of 30% by volume for majorite, yields ~180 ppm wt H₂O stored by majorite at 410 km depth. Such amount is comprised in the uncertainty of our estimation at 410 km depth (see Fig. 10). But again this demonstrates the need to measure the solubility of water in garnet/majorite at high-pressures and temperatures.

Finally, the present study shows that at 410 km the upper mantle can store around 1000 ppm wt H₂O, if water is exclusively stored in the 60 vol% made of olivine. This is of course a minimum since the other phases are unlikely to be completely dry. Considering all the assumptions listed above a maximum storage capacity of the upper mantle at 410 km depth is of 1500 ± 300 ppm wt water (see Fig. 10). This value is lower than

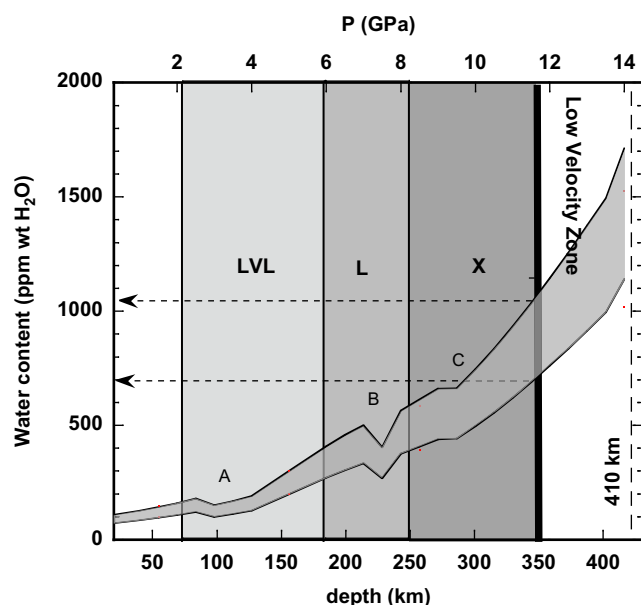


Fig. 10. Water saturation of the upper mantle as a function of depth (shown as the gray zone). It implies a maximum storage capacity comprised between 1200 and 1800 ppm wt H₂O at the 410 km discontinuity. The various seismic features of the upper mantle are shown as the LVL or Low Velocity Layer, the L or Lehmann discontinuity, the X or X-discontinuity, the Low velocity layer at 350 km, as well as the 410 km-depth discontinuity. The kinks in the curves **A**, **B** and **C** are discussed in the text. The two horizontal arrows point out to the range of water content in the mantle necessary to reach the water storage capacity, hence to melt the mantle and form a Low Velocity Layer around 350 km depth.

previous estimates (Bolfan-Casanova, 2005) due to the integration of the effect of temperature on water activity drop.

6. Geophysical implications

Recently, Tauzin et al. (2010) conducted a global study on P to S wave conversion. Their results show the global existence of a low velocity layer (LVL), located at 350 km depth. The occurrence of such LVL is interpreted as linked to melting occurrence. Several factors can be invoked to explain the formation of melt at this depth: (1) an abnormally high temperature, which may be caused by the presence of a mantle plume, and consequently provoke the crossing of the mantle solidus, (2) the release of an aqueous fluid, caused by dehydration of hydrated minerals in subducting slabs, or (3) the fact that the uprising mantle exceeds its water storage capacity. The seismic survey conducted by Tauzin et al. (2010) shows that the LVL is not observed in a particular geodynamic setting, as mantle plumes or subduction zones, but instead is present on a global scale. The global character of the LVL is thus most probably caused by the release of fluid causing crossing of the solidus when the water storage capacity of the mantle is exceeded. If this is the case, then the depth of the LVL can in turn provide a unique insight on the water content of the upper mantle. Examination of Fig. 10 shows that the water storage capacity of the upper mantle at 350 km depth is comprised between 700 and 1000 ppm wt H₂O. Melting at 350 km depth thus indicates that the mantle contains at that depth 850 ± 150 ppm wt H₂O. This is much higher than the estimations of the water content in the source of Mid Oceanic Ridge basalts (MORB) that range between 50 and 200 ppm wt H₂O (Dixon et al., 1988; Michael, 1988; Sobolev and Chaussidon, 1996; Saal et al., 2002). Our estimate is also higher than the higher estimates of 500 ppm wt H₂O (see Yoshino, 2010; Karato, 2011; Khan and

Shankland, 2012) based on electrical conductivity studies. Compared to a water budget of 1500–2700 ppm wt for the whole planet as inferred from geochemical and cosmochemical grounds (Jambon and Zimmermann, 1990; Marty, 2012), our estimation implies that the deep Earth should contain more water than the upper mantle. Note that the present water storage capacity curve predicts ~ 300 ppm wt H₂O at depths corresponding to the source of MORB (2–3 GPa), a value in agreement with measurements on ridge basalts (see above).

6.1. Relation to the seismic structure of the upper mantle

Also, Fig. 10 reveals several features or negative kinks (named **A**, **B** and **C**) in the water storage capacity of the upper mantle. Of course, we have to be careful that such features are not calculation artefacts introduced by the numerous assumptions made in our model. Still, we notice that at low-pressures the negative kink **A** in water storage capacity observed between 75 and 130 km depth coincides with a seismic Low-Velocity Zone (the onset of the asthenosphere). This observation was previously made by Mierdel et al. (2007) and was explained by a lower Al solubility in pyroxene at such depths compared to the solubility at shallower depths. The interpretation is that the drop in Al content induces a dehydration of pyroxene that triggers melting, thus causing a decrease in the seismic velocities. This previous petrological explanation is in excellent agreement with the results of our experiments: with increasing pressure, Al content in pyroxene decreases hence the water partitioning into this phase decreases. Of course, the **A** feature is enhanced in our model because the calculation implies a sudden change of $D_{\text{opx/olivine}}^{\text{water}}$ that goes from 2 to 0.9 at 2.5 GPa (80 km) and 1300 °C.

The seismic structure of the Earth's upper mantle displays several other features among which the Lehmann and X discontinuities are not understood yet. Both designate sharp velocity increases in the range of 180–240 km for the L-discontinuity and in the range of 240–340 km for the X-discontinuity (Bagley and Revenaugh, 2008; Deuss and Woodhouse, 2004). Concerning the L-discontinuity, it displays a clearly negative seismological clapeyron slope, (Deuss and Woodhouse, 2004), which, in the absence of any analog in silicate phase transitions, was interpreted as due to a transition from dislocation creep to diffusion creep regime of deformation. On the other hand, the X-discontinuity does not show a clear sign in clapeyron slope (Deuss and Woodhouse, 2004). There are at present two candidate phase transitions that were thought to occur at pressure and temperature conditions corresponding to the depth-range observed for the X discontinuity: namely the coesite/stishovite transition (Williams and Revenaugh, 2005) and the orthoenstatite/clinoenstatite (Angel et al., 1992; Woodland, 1998). Still, explaining the X discontinuity by the phase transition in silica implies substantial amounts of eclogite material within the mantle, which is not sampled by MORBs. The variability in depth and geological setting of both discontinuities are also not easily explained by thermal heterogeneities since a 600–800 °C lateral variation is required (Jacobsen et al., 2010). Rather, the depth variability could reflect chemical heterogeneities (including degree of fertility and water content). As already mentioned, recent experiments in the pure MgSiO₃ end-member have shown that the addition of water shifts the orthoenstatite to clinoenstatite (Withers and Hirschmann, 2007) and Low Pressure clinoenstatite to High Pressure clinoenstatite (Bromiley and Bromiley, 2006) to lower pressures, due to the larger water storage capacity of the high-pressure polymorphs. The same should be expected for the coesite–stishovite transition considering that Al-bearing stishovite dissolves more water than coesite (Mosenfelder, 2000; Litasov et al., 2007). Recent re-examination of the orthoenstatite to clinoenstatite

transition in the MgSiO_3 end member has established that for a normal mantle geotherm the transition should occur at ~ 8.5 GPa (i.e. ~ 260 km depth), in a nominally dry system, which corresponds to the onset of the X-discontinuity (240–340 km) (see Akashi et al., 2009). Considering the effect of iron in lowering the pressure of the transition (Ross and Reynard, 1999) as well as the effect of hydrogen (Withers and Hirschmann, 2007), the orthoenstatite to clinoenstatite phase transition in a hydrous mantle should start well above 260 km depth. We have seen in this study that $(\text{Mg,Fe,Al})(\text{Si,Al})\text{O}_3$ pyroxene is already monoclinic at 7.5 GPa, that is ~ 230 km, thus the orthoenstatite to clinoenstatite transition is depressed at least as much in the Fe and Al bearing system than in the pure MSH system. This implies that the X discontinuity (240–340 km depth) is difficult to reconcile with the orthoenstatite to clinoenstatite phase transition in a hydrous mantle. We thus agree with Jacobsen et al. (2010) that the orthoenstatite to clinoenstatite transition in a hydrous mantle should rather occur at depths corresponding to the bottom of the L-discontinuity (180–240 km depth). The negative clapeyron slope of this discontinuity could then be explained by variations in water content. As shown in Fig. 10, the L-discontinuity coincides with a negative kink in the water storage capacity of the upper mantle, denoted as feature B, centered at 230 km depth. This feature arises in the calculation from a change in partition coefficient between high-Ca pyroxene and low-Ca pyroxene across the orthorhombic to monoclinic transition in enstatite. The kink can be more or less pronounced depending on the magnitude of the change in $D_{\text{Ca-rich pyroxene/Ca-poor pyroxene}}^{\text{water}}$ through the phase transition. The X-discontinuity coincides in Fig. 10 with feature C around 280 km depth, denoting a flattening of the water storage capacity curve that arises in the calculation from the dehydration of garnet.

7. Conclusions

By performing experiments up to 13.5 GPa and 1400 °C, we confirm that water solubility in NAMs increases with pressure but decreases with increasing temperature. This study also brings new observations about the effect of aluminum on the incorporation of water in pyroxene and olivine, with effects that depend on pressure and could not have been extrapolated from low pressure data. Also, the effect of aluminum on the partitioning of water between enstatite and olivine is shown to change significantly with pressure, decreasing it from 2 at 2.5 GPa (80 km depth) to 0.9 at 9 GPa (270 km depth) in the MFASH system, concomitantly to the decrease in Al content of pyroxene with increasing pressure. At 13.5 GPa and 1400 °C, the water content of olivine is 1700 ± 300 ppm wt H_2O , with a preferred partition coefficient of 4.7 ± 0.7 in wadsleyite. These data are used, together with assumptions on water partitioning into Ca-clinopyroxene and water solubility in garnet, to build a water saturation curve for the upper mantle. We conclude that the water storage capacity of the upper mantle reaches 1500 ± 300 ppm wt H_2O just above the 410 km discontinuity. Finally, if the Low Velocity Layer (LVL) observed near 350 km is indeed due to melting of the mantle, it can constrain the water content of the mantle at that depth to be $\sim 850 \pm 150$ ppm wt H_2O , which is four times higher than the water content estimated for the mantle source of Mid Oceanic Ridge Basalts.

Finally, comparison of the depth ranges of the L and X seismic discontinuities and the water storage capacity curve of the upper mantle suggests that the L-discontinuity (180–240 km) is concomitant with a kink in the water storage due to the orthorhombic to monoclinic phase transition in enstatite, while the

X-discontinuity (240–340 km) coincides with a kink in the water storage capacity due to dehydration of garnet.

Acknowledgments

This study was funded by INSU Diety program. It is part of the Ph.D. thesis of A. Férot. We thank J.-L. Fruquière for machining multi-anvil parts, F. Pointud and F. Doré for mechanical and electronical assistance, J.-L. Devidal for running the electron probe and J.-M. Hénot for the SEM apparatus. This manuscript was greatly improved by the meticulous reviews from J. Mosenfelder, A. Withers and M. Koch-Müller. This is CLERVOLC contribution no. 24.

Appendix A. Supporting information

Supplementary data associated with this article can be found in the online version at <http://dx.doi.org/10.1016/j.epsl.2012.06.022>.

References

- Akaogi, M., Yusa, H., Shiraishi, K., Suzuki, T., 1995. Thermodynamic properties of alpha-quartz, coesite, and stishovite and equilibrium phase-relations at high-pressures and high-temperatures. *J. Geophys. Res.—Solid Earth* 100, 22337–22347.
- Akashi, A., Nishihara, Y., Takahashi, E., Nakajima, Y., Tange, Y., Funakoshi, K., 2009. Orthoenstatite/clinoenstatite phase transformation in MgSiO_3 at high-pressure and high-temperature determined by in situ X-ray diffraction: implications for nature of the X discontinuity. *J. Geophys. Res.—Solid Earth*, 114.
- Angel, R.J., Hughes, D.A., 1994. Equations of state and thermodynamic properties of enstatite pyroxenes. *J. Geophys. Res.—Solid Earth* 99, 19777–19783.
- Angel, R.J., Chopelas, A., Ross, N.L., 1992. Stability of high-density clinoenstatite at upper-mantle pressures. *Nature* 358, 322–324.
- Asimow, P.D., Stein, L.C., Mosenfelder, J.L., Rossman, G.R., 2006. Quantitative polarized FTIR analysis of trace OH in populations of randomly oriented mineral grains. *Am. Mineral.*, 278–284.
- Aubaud, C., Hauri, E.H., Hirschmann, M.M., 2004. Hydrogen partition coefficients between nominally anhydrous minerals and basaltic melts. *Geophys. Res. Lett.*
- Bagley, B., Revenaugh, J., 2008. Upper mantle seismic shear discontinuities of the Pacific. *J. Geophys. Res.—Solid Earth*, 113.
- Bai, Q., Kohlstedt, D.L., 1992. Substantial hydrogen solubility in olivine and implications for water storage in the mantle. *Nature*, 672–674.
- Bai, Q., Kohlstedt, D.L., 1993. Effects of chemical environment on the solubility and incorporation mechanism for hydrogen in olivine. *Phys. Chem. Miner.*, 460–471.
- Balan, E., Ingrin, J., Delattre, S., Kovacs, I., Blanchard, M., 2011. Theoretical infrared spectrum of OH-defects in forsterite. *Eur. J. Mineral.* 23, 285–292.
- Bali, E., Bolfan-Casanova, N., Koga, K.T., 2008. Pressure and temperature dependence of H solubility in forsterite: an implication to water activity in the Earth interior. *Earth Planet. Sci. Lett.* 268, 354–363.
- Bell, D.R., Rossman, G.R., 1992. Water in Earth's mantle: the role of nominally anhydrous minerals. *Science*, 1391–1397.
- Bell, D.R., Ithigher, P.D., Rossman, G.R., 1995. Quantitative analysis of trace OH in garnet and pyroxenes. *Am. Mineral.*, 465–474.
- Bell, D.R., Rossman, G.R., Moore, R.O., 2004. Abundance and partitioning of OH in a high-pressure magmatic system: megacrysts from the Monastery Kimberlite, South Africa. *J. Petrol.*, 1539–1564.
- Bell, D.R., Rossman, G.R., Maldener, A., Endisch, D., Rauch, F., 2003. Hydroxide in olivine: a quantitative determination of the absolute amount and calibration of the IR spectrum. *J. Geophys. Res.*, 2106.
- Berry, A., Hermann, J., O'Neill, H.S.C., Foran, G.J., 2005. Fingerprinting the water site in mantle olivine. *Geology* 869–872, <http://dx.doi.org/10.1130/G21759.1>.
- Berry, A.J., O'Neill, H.S.C., Hermann, J., Scott, D.R., 2007. The infrared signature of water associated with trivalent cations in olivine. *Earth Planet. Sci. Lett.* 261, 134–142.
- Bolfan-Casanova, N., 2005. Water in the Earth's mantle. *Mineral. Mag.* 69, 227–255.
- Bolfan-Casanova, N., Keppler, H., Rubie, D.C., 2000. Water partitioning between nominally anhydrous minerals in the $\text{MgO-SiO}_2\text{-H}_2\text{O}$ system up to 24 GPa: implications for the distribution of water in the Earth's mantle. *Earth Planet. Sci. Lett.* 182, 209–221.
- Bolfan-Casanova, N., Munoz, M., McCammon, C., Deloule, E., Férot, A., Demouchy, S., France, L., Andrault, D., Pascarelli, S. Ferric iron and water incorporation in wadsleyite under hydrous and oxidizing conditions: a XANES, Mössbauer and SIMS study. *Am. Mineral.*, <http://dx.doi.org/10.2138/am.2012.3869>, in press.

- Bromiley, G.D., Bromiley, F.A., 2006. High-pressure phase transitions and hydrogen incorporation into MgSiO_3 enstatite. *Am. Mineral.* 91, 1094–1101.
- Chai, M., Brown, J.M., Slutsky, L.J., 1997. The elastic constants of an aluminous orthopyroxene to 12.5 GPa. *J. Geophys. Res.—Solid Earth* 102, 14779–14785.
- Chen, J.H., Inoue, T., Yurimoto, H., Weidner, D.J., 2002. Effect of water on olivine-wadsleyite phase boundary in the $(\text{Mg}, \text{Fe})_2\text{SiO}_4$ system. *Geophys. Res. Lett.* 29.
- Demouchy, S., Delouie, E., Frost, D.J., Keppler, H., 2005. Pressure and temperature-dependence of water solubility in Fe-free wadsleyite. *Am. Mineral.* 90, 1084–1091.
- Demouchy, S., Jacobsen, S., Gaillard, F., Stern, C., 2006. Rapid magma ascent recorded by water diffusion profiles in mantle olivine. *Geology*, 429–432.
- Deon, F., Koch-Müller, M., Rhede, D., Gottschalk, M., Wirth, R., Thomas, S.M., 2010. Location and quantification of hydroxyl in wadsleyite: new insights. *Am. Mineral.* 95, 312–322.
- Deon, F., Koch-Müller, M., Rhede, D., Wirth, R., 2011. Water and iron effect on the P – T coordinates of the 410-km discontinuity in the Earth's upper mantle. *Contrib. Mineral. Petrol.* (doi:10.1007/s00410-010-0555-6).
- Deuss, A., Woodhouse, J.H., 2004. The nature of the Lehmann discontinuity from its seismological Clapeyron slopes. *Earth Planet. Sci. Lett.* 225, 295–304.
- Dixon, J.E., Stolper, E., Delaney, J.R., 1988. Infrared spectroscopic measurements of CO_2 and H_2O in Juan de Fuca Ridge basaltic glasses. *Earth Planet. Sci. Lett.* 87–104.
- Fisher, G.W., Medaris, L.G., 1969. Cell dimensions and X-ray determinative curve for synthetic Mg–Fe olivines. *Am. Mineral.* 54, 741–753.
- Frost, D.J., Dolejs, D., 2007. Experimental determination of the effect of H_2O on the 410-km seismic discontinuity. *Earth Planet. Sci. Lett.* 256, 182–195.
- Gaetani, G.A., Grove, T.L., 1998. The influence of water on melting of mantle peridotite. *Contrib. Mineral. Petrol.* 323–346.
- Gasparik, T., 2003. Phase Diagrams for Geoscientists. An Atlas of the Earth's Interior. Springer-Verlag, Berlin, Heidelberg, New York (462 pp.).
- Grant, K.J., Kohn, S.C., Brooker, R.A., 2007. The partitioning of water between olivine, orthopyroxene and melt synthesised in the system albite–forsterite– H_2O . *Earth Planet. Sci. Lett.* 260, 227–241.
- Hazen, R.M., Weinberger, M.B., Yang, H.X., Prewitt, C.T., 2000. Comparative high-pressure crystal chemistry of wadsleyite, β -($\text{Mg}_{1-x}\text{Fe}_x$) $_2\text{SiO}_4$, with $x=0$ and 0.25. *Am. Mineral.* 85, 770–777.
- Hirth, G., Kohlstedt, D.L., 1996. Water in the oceanic upper mantle: implications for rheology, melt extraction and the evolution of the lithosphere. *Earth Planet. Sci. Lett.* 93–108.
- Hugh-Jones, D.A., Angel, R.J., 1997. Effect of Ca^{2+} and Fe^{2+} on the equation of state of MgSiO_3 orthopyroxene. *J. Geophys. Res.—Solid Earth* 102, 12333–12340.
- Inoue, T., 1994. Effect of water on melting phase relations and melt composition in the system Mg_2SiO_4 – MgSiO_3 – H_2O up to 15 GPa. *Phys. Earth Planet. Inter.* 237–263.
- Inoue, T., Yurimoto, H., Kudoh, Y., 1995. Hydrous modified spinel, $\text{Mg}_{1.75}\text{Si}_{0.50}\text{O}_4$: a new water reservoir in the mantle transition zone. *J. Geophys. Res.* 117–120.
- Irfune, T., 1987. An experimental investigation of the pyroxene–garnet transformation in a pyrolite composition and its bearing on the constitution of the mantle. *Phys. Earth Planet. Inter.* 324–336.
- Irfune, T., Isshiki, M., 1998. Iron partitioning in a pyrolite mantle and the nature of the 410-km discontinuity. *Nature*, 702–705.
- Jacobsen, S.D., Liu, Z.X., Ballaran, T.B., Littlefield, E.F., Ehm, L., Hemley, R.J., 2010. Effect of H_2O on upper mantle phase transitions in MgSiO_3 : is the depth of the seismic X-discontinuity an indicator of mantle water content? *Phys. Earth Planet. Inter.* 183, 234–244.
- Jambon, A., Zimmermann, J.L., 1990. Water in oceanic basalts: evidence for dehydration of recycled crust. *Earth Planet. Sci. Lett.* 323–331.
- Jamtveit, B., Brooker, R., Brooks, K., Larsen, L.M., Pedersen, T., 2001. The water content of olivines from the North Atlantic Volcanic Province. *Earth Planet. Sci. Lett.* 186, 401–415.
- Karato, S., 2011. Water distribution across the mantle transition zone and its implications for global material circulation. *Earth Planet. Sci. Lett.* 301, 413–423.
- Katsura, T., Yamada, H., Nishikawa, O., Song, M., Kubo, A., Shinmei, T., Yokoshi, S., Aizawa, Y., Yoshino, T., Walter, M.J., Ito, E., Funakoshi, K., 2004. Olivine–wadsleyite transition in the system $(\text{Mg}, \text{Fe})_2\text{SiO}_4$. *J. Geophys. Res.* 109, <http://dx.doi.org/10.1029/2003JB002438>.
- Kawamoto, T., 2004. Hydrous phase stability and partial melt chemistry in H_2O -saturated KLB-1 peridotite up to the uppermost lower mantle conditions. *Phys. Earth Planet. Inter.* 143, 387–395.
- Keppler, H., Bolfan-Casanova, N., 2006. Thermodynamics of water solubility and partitioning. In: Keppler, H., Smyth, J.R., (Eds.), *Reviews in Mineralogy*, vol. 62. Mineralogical Society of America.
- Khan, A., Shankland, T.J., 2012. A geophysical perspective on mantle water content and melting: inverting electromagnetic sounding data using laboratory-based electrical conductivity profiles. *Earth Planet. Sci. Lett.* 317, 27–43.
- Kohlstedt, D.L., Keppler, H., Rubie, D.C., 1996. Solubility of water in the α , β , and γ phases of $(\text{Mg}, \text{Fe})_2\text{SiO}_4$. *Contrib. Mineral. Petrol.* 345–357.
- Kovacs, I., O'Neill, H.S.C., Hermann, J., Hauri, E.H., 2011. Site-specific infrared O–H absorption coefficients for water substitution into olivine. *Am. Mineral.* 95, 292–299.
- Kovacs, I., Hermann, J., O'Neill, H.S.C., Gerald, J.F., Sambridge, M., Horvath, G., 2008. Quantitative absorbance spectroscopy with unpolarized light: part II. Experimental evaluation and development of a protocol for quantitative analysis of mineral IR spectra. *Am. Mineral.* 93, 765–778.
- Kudoh, Y., Kuribayashi, T., Kagi, H., Inoue, T., 2006. Cation vacancy and possible hydrogen positions in hydrous forsterite, $\text{Mg}_{1.985}\text{Si}_{0.993}\text{H}_{0.06}\text{O}_4$, synthesized at 13.5 GPa and 1300 degrees C. *J. Mineral. Petrol. Sci.* 101, 265–269.
- Lemaire, C., Kohn, S.C., Brooker, R.A., 2004. The effect of silica activity on the incorporation mechanisms of water in synthetic forsterite: a polarised infrared spectroscopic study. *Contrib. Mineral. Petrol.* 48–57.
- Libowitzky, E., Rossman, G.R., 1996. Principles of quantitative absorbance measurements in anisotropic crystals. *Phys. Chem. Miner.* 319–327.
- Litasov, K.D., Shatskiy, A., Ohtani, E., Katsura, T., 2011. Systematic study of hydrogen incorporation into Fe-free wadsleyite. *Phys. Chem. Miner.* 38, 75–84.
- Litasov, K.D., Ohtani, E., Kagi, H., Jacobsen, S.D., Ghosh, S., 2007. Temperature dependence and mechanism of hydrogen incorporation in olivine at 12.5–14.0 GPa. *Geophys. Res. Lett.* 34.
- Liu, X., Wang, Y., Liebermann, R.C., Maniar, P.D., Navrotsky, A., 1991. Phase-transition in Cageo3 Perovskite—evidence from X-ray-powder diffraction, thermal-expansion and heat-capacity. *Phys. Chem. Miner.* 18, 224–230.
- Lu, R., Keppler, H., 1997. Water solubility in pyrope to 100 kbar. *Contrib. Mineral. Petrol.* 35–42.
- Marty, B., 2012. The origins and concentrations of water, carbon, nitrogen and noble gases on Earth. *Earth Planet. Sci. Lett.* 313–314, 56–66.
- Matveev, S., O'Neill, H.S.C., Ballhaus, C., Taylor, W.R., Green, D.H., 2001. Effect of silica activity on OH–IR spectra of olivine: implications for low- aSiO_2 mantle metasomatism. *J. Petrol.* 721–729.
- McKenzie, D., Bickle, M.J., 1988. The volume and composition of melt generated by extension of the lithosphere. *J. Petrol.* 29, 625–679.
- Mei, S., Kohlstedt, D.L., 2000. Influence of water on plastic deformation of olivine aggregates 1. Diffusion creep regime. *J. Geophys. Res.* 21457–21469.
- Mibe, K., Kanzaki, M., Kawamoto, T., Kyoko, M.N., Fei, Y., Ono, S., 2007. Second critical endpoint in the peridotite– H_2O system. *J. Geophys. Res.* <http://dx.doi.org/10.1029/2005JB004125>.
- Michael, P.J., 1988. The concentration, behavior and storage of H_2O in the sub-oceanic upper mantle: implications for mantle metasomatism. *Geochim. Cosmochim. Acta*, 555–566.
- Mierdel, K., Keppler, H., 2004. The temperature dependence of water solubility in enstatite. *Contrib. Mineral. Petrol.*
- Mierdel, K., Keppler, H., Smyth, J.R., Langenhorst, F., 2007. The origin of the Earth's asthenosphere. *Science*, 364–368.
- Mookerjee, M., Karato, S., 2010. Solubility of water in pyrope-rich garnet at high pressures and temperature. *Geophys. Res. Lett.* 37.
- Morishima, H., Kato, T., Suto, M., Kikegawa, T., S.U.W.U.O.S., 1994. The phase boundary between α - and β - Mg_2SiO_4 determined by in situ X-ray observation. *Science*, 1202–1203.
- Mosenfelder, J.L., 2000. Pressure dependence of hydroxyl solubility in coesite. *Phys. Chem. Miner.* 27, 610–617.
- Mosenfelder, J.L., Deligne, L.L., Asimow, P.D., Rossman, G.R., 2006. Hydrogen incorporation in olivine from 2–12 GPa. *Am. Mineral.* 285–294.
- Ohtani, E., Mizobata, H., Yurimoto, H., 2000. Stability of dense hydrous magnesium silicate phases in the systems Mg_2SiO_4 – H_2O and MgSiO_3 – H_2O at pressures up to 27 GPa. *Phys. Chem. Miner.* 533–544.
- O'Neill, H.S.C., Rubie, D.C., Canil, D., Geiger, C.A., Ross, I.C.R., Seifert, F., Woodland, A., 1996. Ferric iron in the upper mantle and in transition zone assemblages: implications for relative oxygen fugacities in the mantle. In: Takahashi, E., Jeanloz, R., Rubie, D.C. (Eds.), *Evolution of the Earth and Planets*, vol. 74, AGU Monograph.
- Peslier, A.H., 2010. A review of water contents of nominally anhydrous natural minerals in the mantles of Earth, Mars and the Moon. *J. Volcanol. Geotherm. Res.* 197, 239–258.
- Peslier, A.H., Luhr, J.F., Post, J., 2002. Low water contents in pyroxenes from spinel-peridotites of the oxidized, sub-arc mantle wedge. *Earth Planet. Sci. Lett.* 69–86.
- Pownceby, M.I., O'Neill, H.S.C., 1994. Thermodynamic data from redox reactions at high temperatures. IV. Calibration of the Re– ReO_2 oxygen buffer from EMF and NiO+Ni–Pd redox sensor measurements. *Contrib. Mineral. Petrol.* 130–137.
- Prechtel, F., Stalder, R., 2012. OH-defects in Al- and Cr-doped synthetic enstatites and defect geobarometry on natural orthopyroxenes from the Earth's mantle. *Eur. J. Mineral.* 24, 471–481.
- Rauch, M., Keppler, H., 2002. Water solubility in orthopyroxene. *Contrib. Mineral. Petrol.*
- Robinson, J.A.C., Wood, B.J., 1998. The depth of the spinel to garnet transition at the peridotite solidus. *Earth Planet. Sci. Lett.* 164, 277–284.
- Ross, N.L., Reynard, B., 1999. The effect of iron on the $P_2(1)/c$ to C_2/c transition in $(\text{Mg}, \text{Fe})\text{SiO}_3$ clinopyroxenes. *Eur. J. Mineral.* 11, 585–589.
- Saal, A.E., Hauri, E.H., Langmuir, C.H., Perfit, M.R., 2002. Vapour undersaturation in primitive mid-ocean-ridge basalt and the volatile content of Earth's upper mantle. *Nature*, 451–455.
- Smyth, J.R., Frost, D.J., Nestola, F., Holl, M., Bromiley, G., 2006. Olivine hydration in the deep upper mantle: effects of temperature and silica activity. *Geophys. Res. Lett.* 33, <http://dx.doi.org/10.1029/2006GL026194>.
- Sobolev, A.V., Chaussidon, M., 1996. H_2O concentrations in primary melts from supra-subduction zones and mid ocean ridges: implications for H_2O storage and recycling in the mantle. *Earth Planet. Sci. Lett.* 45–55.
- Stalder, R., 2004. Influence of Fe, Cr, and Al on hydrogen incorporation in orthopyroxene. *Eur. J. Mineral.* 703–711.
- Stalder, R., Skogby, H., 2002. Hydrogen incorporation in enstatite. *Eur. J. Mineral.* 1139–1144.

- Stalder, R., Ulmer, P., Thompson, A.B., Günther, D., 2001. High pressure fluids in the systems $\text{MgO-SiO}_2\text{-H}_2\text{O}$ under upper mantle conditions. *Contrib. Mineral. Petrol.* 150, 607–618.
- Stalder, R., Klemme, S., Ludwig, T., Skogby, H., 2005. Hydrogen incorporation in orthopyroxene: interaction of different trivalent cations. *Contrib. Mineral. Petrol.* 150, 473–485.
- Tauzin, B., Debayle, E., Wittlinger, G., 2010. Seismic evidence for a global low-velocity layer within the Earth's upper mantle. *Nat. Geosci.* 3, 718–721.
- Tenner, T.J., Hirschmann, M.M., Withers, A.C., Hervig, R.L., 2009. Hydrogen partitioning between nominally anhydrous upper mantle minerals and melt between 3 and 5 GPa and applications to hydrous peridotite partial melting. *Chem. Geol.* 262, 42–56.
- Tenner, T.J., Hirschmann, M.M., Withers, A.C., Ardia, P., 2012. H_2O storage capacity of olivine and low-Ca pyroxene from 10 to 13 GPa: consequences for dehydration melting above the transition zone. *Contrib. Mineral. Petrol.* 163, 297–316.
- Umemoto, K., Wentzcovitch, R.M., Hirschmann, M.M., Kohlstedt, D.L., Withers, A.C., 2011. A first-principles investigation of hydrous defects and IR frequencies in forsterite: the case for Si vacancies. *Am. Mineral.* 96, 1475–1479.
- Williams, Q., Revenaugh, J., 2005. Ancient subduction, mantle eclogite, and the 300 km seismic discontinuity. *Geology* 33, 1–4.
- Withers, A.C., Hirschmann, M.M., 2007. H_2O storage capacity of MgSiO_3 clinoenstatite at 8–13 GPa, 1100–1400 degrees C. *Contrib. Mineral. Petrol.* 154, 663–674.
- Withers, A.C., Hirschmann, M.M., 2008. Influence of temperature, composition, silica activity and oxygen fugacity on the H_2O storage capacity of olivine at 8 GPa. *Contrib. Mineral. Petrol.* 156, 595–605.
- Withers, A.C., Wood, B.J., Carroll, M.R., 1998. The OH content of pyrope at high pressure. *Chem. Geol.* 161–171.
- Withers, A.C., Hirschmann, M.M., Tenner, T.J., 2011. The effect of Fe on olivine H_2O storage capacity: consequences for H_2O in the martian mantle. *Am. Mineral.* 96, 1039–1053.
- Woodland, A.B., 1998. The orthorhombic to high-P monoclinic phase transition in Mg-Fe pyroxenes: can it produce a seismic discontinuity? *Geophys. Res. Lett.* 25, 1241–1244.
- Yoshino, T., 2010. Laboratory electrical conductivity measurement of mantle minerals. *Surv. Geophys.* 31, 163–206.
- Zhang, J., Li, B., Utsumi, W., Liebermann, R.C., 1996. In situ X-ray observations of the coesite stishovite transition: reversed phase boundary and kinetics. *Phys. Chem. Miner.* 23, 1–10.
- Zhao, Y.H., Ginsberg, S.B., Kohlstedt, D.L., 2004. Solubility of hydrogen in olivine: dependence on temperature and iron content. *Contrib. Mineral. Petrol.* 155–161.